SIAM J. Applied Dynamical Systems
Vol. 1, No. 2, pp. 248–270


# Numerical Bifurcation Analysis for Multisection Semiconductor Lasers*

Jan Sieber†

**Abstract.** We investigate the dynamics of a multisection laser implementing a delayed optical feedback experiment where the length of the cavity is comparable to the length of the laser. First, we reduce the traveling-wave model with gain dispersion (a hyperbolic system of PDEs) to a system of ODEs describing the semiflow on a local center manifold. Then we analyze the dynamics of the system of ODEs using numerical continuation methods (AUTO). We explore the plane of the two parameters—feedback phase and feedback strength—to obtain a bifurcation diagram for small and moderate feedback strength. This diagram permits us to understand the roots of a variety of nonlinear phenomena observed numerically and experimentally such as, e.g., self-pulsations, excitability, hysteresis, or chaos, and to locate them in the parameter plane.

**Key words.** semiconductor lasers, delayed optical feedback, numerical bifurcation analysis

**AMS subject classifications.** 34C60, 78A60

**PII.** S1111111102401746

## 1. Introduction.

Semiconductor lasers subject to delayed optical feedback show a variety of nonlinear effects. Self-pulsations, excitability, coexistence of several stable regimes, and chaotic behavior have been observed in both experiments and numerical simulations [5], [13], [19], [24], [28]. Multisection lasers allow us to design and control these feedback effects and permit their application, e.g., in optical data transmission, processing, and recovery [24], [34].

If mathematical modeling is to be helpful in guiding this difficult and expensive design process, it has to meet two criteria that contradict each other. On one hand, the model should be accurate, and its parameters should be directly accessible for experimenters. Typically, only very complex models allow for that, e.g., systems of PDEs.

On the other hand, the modeling should permit insight into the nature of the nonlinear effects. This is often impossible using only simulations, i.e., performing the experiment at the computer. Only a detailed bifurcation analysis allows us to find coexisting stable regimes, unstable objects which are boundaries of coexisting attracting regions, and bifurcations of higher codimension which are a common source for various nonlinear phenomena. Unfortunately, there exist numerical bifurcation tools only for low-dimensional ODEs [11], [16] and very restricted classes of PDEs, e.g., delay-differential equations [12].

In this paper, we start from the traveling-wave model [2], [18], [29], which resolves the light amplitude $E$ within the laser spatially in the longitudinal direction but treats the carrier density $n$ as a spatially sectionwise averaged quantity. For illustrative purposes, we restrict

*Received by the editors February 1, 2002; accepted for publication by B. Krauskopf June 18, 2002; published electronically November 6, 2002. This work was supported by the Sonderforschungsbereich 555 "Komplexe Nichtlineare Prozesse" of the Deutsche Forschungsgemeinschaft.
http://www.siam.org/journals/siads/1-2/40174.html
†Humboldt University, Berlin, Germany, and Weierstrass Institute for Applied Analysis and Stochastics, Mohrenstraße 39, D-10117 Berlin, Germany (sieber@wias-berlin.de).

our analysis to a particular multisection laser configuration implementing a classical delayed optical feedback experiment (see Figure 1). This way, the model has the structure

$$\begin{aligned} \dot{E} &= H(n)E, \\ \dot{n} &= \varepsilon\left(f(n) - g(n)[E,E]\right), \end{aligned} \tag{1.1}$$

where the first equation is a hyperbolic linear system of PDEs for $E$ which is nonlinearly coupled with one scalar ODE for $n$. This model is particularly well adapted to multisection lasers: It is sufficiently accurate to keep track of the effects caused by the longitudinal resonator structure within the laser. On the other hand, the parameter $\varepsilon$ is small. This slow-fast structure permits us to derive analytically low-dimensional systems of ODEs (*mode approximations* [2], [5], [34]) which approximate the semiflow on a local center manifold [26], [32]. These ODEs are accessible for classical numerical bifurcation analysis tools like AUTO. This way we meet both requirements: we present reasonably complete bifurcation diagrams in the physically relevant parameters for a theoretically, and numerically [23], justified approximation of the full system (1.1) of PDEs .

One further remark about the choice of the model: another very popular model for the investigation of delayed optical feedback effects is the Lang–Kobayashi system [13], [17], [19], [30], [28]. It also has the structure of (1.1). Hence it can be treated by the model reduction methods presented in this paper, too. However, we use the traveling-wave model as it fits better to the setting of a multisection laser.

The outline of the paper is as follows: In section 2, we will describe the traveling-wave model in more detail and reiterate the theorem of [26] concerning the model reduction to mode approximations. In section 3, we perform a numerical bifurcation analysis of the *single-mode approximation* (a two-dimensional system of ODEs), which is a valid approximation if the feedback strength is sufficiently small. The primary bifurcation parameters are the feedback strength $\eta$ and the feedback phase $\varphi$. In section 4, we derive an appropriately posed two-mode approximation (a four-dimensional system of ODEs) in the vicinity of a point where the critical eigenvalue of $H(n)$ has algebraic multiplicity two. Furthermore, we perform a numerical bifurcation analysis of this system, thus completing the bifurcation diagram up to higher levels of feedback. However, this system shows complicated dynamics such that the bifurcation analysis remains incomplete. In section 5, we give a brief summary and an outlook to further investigations.

## 2. The mathematical model.

**2.1. The traveling-wave model with gain dispersion.** We consider the geometric configuration presented in Figure 1. Let $\psi(t) \in \mathbb{L}^2([0,L];\mathbb{C}^2)$ describe the spatially resolved complex amplitude of the optical field, which is split into a forward and backward traveling wave. Let $p(t) \in \mathbb{L}^2([0,L];\mathbb{C}^2)$ be the corresponding nonlinear polarization [4], [25]. Denote the one-dimensional spatial variable by $z \in [0,L]$ (the longitudinal direction in the laser). The scalar $n(t) \in \mathbb{R}$ describes the spatially averaged carrier density in the first section $S_1$. Then the traveling-wave model with gain dispersion [4], [25], [26] poses an initial-boundary-value problem for $\psi$, $p$, and $n$ which reads as follows (see the appendix for the physical interpretation

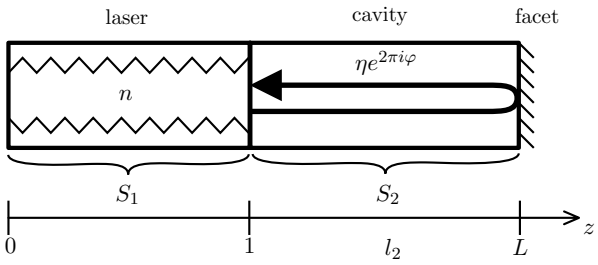


**Figure 1.** *Geometric configuration for the case of a two-section laser. The DFB section $S_1$ (DFB=distributed feedback, i.e., $\kappa(z) \neq 0$ in system (2.1)) acts as a laser. Its spatially averaged carrier density $n$ is a scalar dependent variable. The other section acts as a cavity and provides delayed optical feedback of strength $\eta$ and phase $\varphi$.*

and further references):

$$
\begin{aligned}
\frac{d}{dt}\psi(t,z) &= \sigma\partial_z\psi(t,z) + \beta(n(t),z)\psi(t,z) - i\kappa(z)\sigma_c\psi(t,z) + \rho(z)p(t,z),\\
\frac{d}{dt}p(t,z) &= (i\Omega_r(z) - \Gamma(z))\cdot p(t,z) + \Gamma(z)\psi(t,z),\\
\frac{d}{dt}n(t) &= I - \frac{n(t)}{\tau} - P[(G(n(t)) - \rho_1)(\psi(t),\psi(t))_1 + \rho_1 \operatorname{Re}(\psi(t),p(t))_1],
\end{aligned}
\tag{2.1}
$$

where $\sigma = \left(\begin{smallmatrix} -1 & 0 \\ 0 & 1 \end{smallmatrix}\right)$, $\sigma_c = \left(\begin{smallmatrix} 0 & 1 \\ 1 & 0 \end{smallmatrix}\right)$, and $\psi$ satisfies the reflection boundary conditions

$$
\psi_1(t,0) = r_0\psi_2(t,0), \quad \psi_2(t,L) = r_L\psi_1(t,L),
\tag{2.2}
$$

where $|r_0|, |r_L| < 1$, and $r_0 r_L \neq 0$. For brevity, we introduced the notation

$$
(\psi,\varphi)_1 = \int_0^1 \psi(z)^*\varphi(z)\,dz
$$

for $\psi$, $\varphi \in \mathbb{L}^2([0,L];\mathbb{C}^2)$ in (2.1).

The coefficients $\beta \in \mathbb{C}$, $\kappa \in \mathbb{R}$, $\rho \in \mathbb{R}$, $\Omega_r \in \mathbb{R}$, and $\Gamma \in \mathbb{R}$ ($\rho \geq 0$, $\Gamma > 0$) are sectionwise spatially constant functions. We refer to their value in section $S_k$ by appending the according index, e.g., $\rho_1$. Moreover, $\beta_1$ depends on $n$ in the following way:

$$
\beta_1(n) = \beta_1^0 + (1 + i\alpha_1)G(n) - \rho_1,
\tag{2.3}
$$

where $\beta_1^0 \in \mathbb{C}$, $\operatorname{Re}\beta_1^0 < 0$, and $\alpha_1 > 0$. We assume that $G(n)$ is affine:

$$
G(n) = g_1 \cdot (n-1), \qquad \text{where } g_1 > 0.
\tag{2.4}
$$

It is obvious that system (2.1) has the form (1.1), where $E = (\psi, p)$. The linear differential operator $H(n)$ is defined by

$$
H(n)\begin{pmatrix}\psi\\ p\end{pmatrix} = \begin{pmatrix}\sigma\partial_z + \beta(n) - i\kappa\sigma_c & \rho\\ \Gamma & i\Omega_r - \Gamma\end{pmatrix}\begin{pmatrix}\psi\\ p\end{pmatrix}
\tag{2.5}
$$

and acts from

$$Y := \{(\psi, p) \in \mathbb{H}^1([0,L];\mathbb{C}^2) \times \mathbb{L}^2([0,L];\mathbb{C}^2) : \psi \text{ satisfying (2.2)}\} \tag{2.6}$$

into $X = \mathbb{L}^2([0,L];\mathbb{C}^4)$. The coefficients $\kappa$, $\Gamma$, $\beta(n)$, $\Omega_r$, and $\rho$ are bounded linear operators in $\mathbb{L}^2([0,L];\mathbb{C}^2)$ defined by the corresponding coefficients in (2.1). The hermitian form $g(n)[E,E]$ is defined by

$$g(n)\left[\begin{pmatrix}\psi_1\\ p_1\end{pmatrix}, \begin{pmatrix}\psi_2\\ p_2\end{pmatrix}\right] = \int_0^1 (\psi_1^*(z), p_1^*(z)) \begin{pmatrix} G(n)-\rho_1 & \frac{1}{2}\rho_1 \\ \frac{1}{2}\rho_1 & 0 \end{pmatrix} \begin{pmatrix}\psi_2(z)\\ p_2(z)\end{pmatrix} dz.$$

Finally, we define the small parameter $\varepsilon$ and the function $f(n)$ in (1.1) by $\varepsilon f(n) = I - n/\tau$, observing that $I$ and $\tau^{-1}$ are of order $O(10^{-2})$ (see Table 1 and the appendix).

Time $t$ and space $z$ are scaled in system (1.1) such that the speed of light within the device is 1 and the length of section $S_1$ is 1. Moreover, $n$ is measured in multiples of the *transparency density* (the zero of $G(n)$), and $E$ is scaled such that the factor $P$ in (2.1) is actually $\varepsilon$. In this scaling, we typically have $\Gamma_1 \gg 1$, whereas the real parts of $\beta$ are of order $O(1)$.

Furthermore, we have $\kappa_2 = \rho_2 = 0$ in the particular situation considered in this paper: the feedback is nondispersive (see Figure 1 and the introduction). Hence the amount $\eta$ and the phase $\varphi$ of the feedback from section $S_2$ can be varied by changing the modulus and the phase of $r_L$, and we can set $\beta_2 = \Omega_{r,2} = \Gamma_2 = 0$ without loss of generality.

*Remark.* Several of the assumptions are made only to simplify the presentation. The computations presented in this paper can also be done in a more general framework, e.g., more sections, other coefficients depending on $n$, or nonaffine but monotone $G(n)$.

**2.2. Model reduction.** Under the assumptions of section 2.1, the following statements hold for the evolution system (1.1) (see [26] for proofs in a more general context).

Theorem 2.1 (existence of semiflow). *Let $(E^0, n^0) \in V := \mathbb{L}^2([0,L];\mathbb{C}^4) \times \mathbb{R}$. Then system (1.1) generates a strongly continuous semiflow $S(t,(E^0,n^0))$ in $V$ which depends $C^\infty$ smoothly on its initial values and on all parameters for all $t \geq 0$. If $E^0 \in Y$, then $S(t,(E^0,n^0))$ is a classical solution of (1.1); i.e., $(E(t),n(t)) = S(t,(E^0,n^0))$ is continuously differentiable with respect to $t$, and $E(t) \in Y$ for all $t \geq 0$.*

This theorem is a direct consequence of the theory of strongly continuous semigroups [22] and an a priori estimate exploiting the dissipativity of system (2.1). It guarantees that (1.1) is indeed an infinite-dimensional dynamical system; i.e., its solutions exist for all positive times. The next statement investigates the spectrum of $H(n)$ for fixed $n$ and the strongly continuous group $T(t)$ in $X$ generated by $H$.

Theorem 2.2 (spectral properties of $H(n)$). *Let*

$$\xi > \xi_- := \max\left\{-\Gamma_1, \frac{1}{L}\operatorname{Re}\left(\beta_1 + \frac{1}{2}\log(r_0 r_L)\right)\right\}.$$

*Then $X$ can be decomposed into two $T(t)$-invariant closed subspaces $X = X_+ \oplus X_-$, where $X_+$ is at most finite-dimensional and spanned by the eigenvectors and generalized eigenvectors associated to the eigenvalues of $H$ in the right half-plane $\{\lambda : \operatorname{Re}\lambda \geq \xi\}$. The restriction of $T(t)$ to $X_-$ is bounded according to*

$$\|T(t)|_{X_-}\| \leq M e^{\xi t} \qquad \text{for } t \geq 0$$

*in any norm which is equivalent to the $X$-norm where the constant $M$ depends on the particular choice of the norm. If $\kappa_1 \neq 0$ or $\rho_1 > 0$, the subspace $X_+$ is nontrivial for sufficiently small $|r_0 r_L|$.*

Moreover, we know that the eigenvalues of the operator $H(n)$ can be computed as roots of its characteristic function $h(\cdot, n)$.

Lemma 2.3 (computation of eigenvalues of $H(n)$). *A complex number $\lambda > \xi_-$ is an eigenvalue of $H(n)$ if and only if*

$$0 = h(\lambda, n) = (\eta e^{2\pi i\varphi - 2\lambda l_2}, -1) T_1(1; \lambda, n) \begin{pmatrix} r_0 \\ 1 \end{pmatrix}.$$

*Here, we denoted*

$$T_1(z; \lambda, n) = \frac{e^{-\gamma z}}{2\gamma} \begin{pmatrix} \gamma + \mu + e^{2\gamma z}(\gamma - \mu) & i\kappa_1 \left(1 - e^{2\gamma z}\right) \\ -i\kappa_1 \left(1 - e^{2\gamma z}\right) & \gamma - \mu + e^{2\gamma z}(\gamma + \mu) \end{pmatrix}$$

*for $z \in [0, 1]$, where $\mu = \lambda - \rho_1 \Gamma_1 (\lambda - i\Omega_{r,1} + \Gamma_1)^{-1} - \beta_1(n)$ and $\gamma = \sqrt{\mu^2 + \kappa_1^2}$.*

If $n < 1$, all eigenvalues $\lambda$ of $H(n)$ are in the left half-plane $\{\operatorname{Re}\lambda < 0\}$. For increasing $n$, finitely many of them will cross the imaginary axis if $|r_0 r_l|$ is small, and $\kappa_1 \neq 0$ according to Theorem 2.2. Denote the smallest $n$ where $q \geq 1$ eigenvalues $\lambda$ of $H(n)$ are on the imaginary axis by $n_0$. Typically, the value $n_0$ is referred to as *threshold* carrier density. Choose $\xi < 0$ such that all other non purely-imaginary eigenvalues of $H(n_0)$ lie to the left of the line $\{\operatorname{Re}\lambda = \xi\}$. We denote the space $X_+$ of complex dimension $q$ according to Theorem 2.2 by $X_c(n)$, and we define the spectral projection $P_c(n)$ for $H(n)$ onto $X_c(n)$. $P_c(n)$ depends smoothly on $n$ in a neighborhood of $n_0$. Let $B(n)$ be a smooth basis of $X_c(n)$.

According to [26], the following local center manifold theorem holds in the vicinity of $n_0$.

Theorem 2.4 (model reduction). *Let $k > 2$ be an integer number, and let $C > 0$. Let $\varepsilon_0 > 0$ be sufficiently small and $U$ be a sufficiently small neighborhood of $n_0$ (depending on $C$ and $k$). Define the balls*

$$\begin{aligned} \mathcal{B} &= \{(E_c, n) \in \mathbb{C}^q \times \mathbb{R} : \|E_c\| < C, n \in U\} \subset \mathbb{C}^q \times \mathbb{R} \text{ and} \\ \mathcal{N} &= \{(E, n) \in X \times \mathbb{R} : \|E\| < C, n \in U\} \subset X \times \mathbb{R}. \end{aligned}$$

*Then there exists a manifold $\mathcal{C}$ with the following properties*:

(i) Representation. *$\mathcal{C}$ can be represented as the graph of a map from $\mathcal{B}$ into $\mathcal{N}$ which maps $(E_c, n) \in \mathcal{B}$ to $(B(n)E_c + \varepsilon\nu(E_c, n, \varepsilon), n)$, where $\nu : \mathcal{B} \times (0, \varepsilon_0) \to X$ is $C^k$ with respect to all arguments. Denote the $E$-component of $\mathcal{C}$ by $E_X(E_c, n, \varepsilon) = B(n)E_c + \varepsilon\nu(E_c, n, \varepsilon) \in X$.*

(ii) Invariance. *$\mathcal{C}$ is $S(t, \cdot)$-invariant relative to $\mathcal{N}$ if $\varepsilon < \varepsilon_0$.*

(iii) Exponential attraction. *Let $(E, n)$ be such that $S(t, (E, n)) \in \mathcal{N}$ for all $t \geq 0$. Then there exists an $(E_c, n_c) \in \mathcal{B}$ such that, for some $M > 0$,*

$$\|S(t, (E, n)) - S(t, (E_X(E_c, n_c, \varepsilon), n_c))\| \leq M e^{\xi t} \qquad \text{for all } t \geq 0, \tag{2.7}$$

*and $\xi < 0$ is as defined above.*

(iv) Flow on the manifold. *The values $\nu(E_c, n, \varepsilon)$ are in $Y$, and $P_c\nu = 0$ for all $(E_c, n, \varepsilon) \in \mathcal{B} \times (0, \varepsilon_0)$. The flow on $\mathcal{C}$ is differentiable with respect to $t$ and governed by the system of ODEs*

$$\begin{aligned} \frac{d}{dt}E_c &= H_c(n)E_c + \varepsilon a_1(E_c, n, \varepsilon)E_c + \varepsilon^2 a_2(E_c, n, \varepsilon)\nu, \\ \frac{d}{dt}n &= \varepsilon F(E_c, n, \varepsilon), \end{aligned} \tag{2.8}$$

*where*

$$\begin{aligned} H_c(n) &= B(n)^{-1}H(n)P_c(n)B(n), \\ a_1(E_c, n, \varepsilon) &= -B(n)^{-1}P_c(n)\partial_n B(n)F(E_c, n, \varepsilon), \\ a_2(E_c, n, \varepsilon) &= B^{-1}(n)P_c(n)\partial_n P_c(n)F(E_c, n, \varepsilon), \\ F(E_c, n, \varepsilon) &= f(n) - g(n)\left[E_X(E_c, n, \varepsilon), E_X(E_c, n, \varepsilon)\right]. \end{aligned}$$

*System (2.8) is symmetric with respect to rotation $E_c \to E_c e^{i\varphi}$, and $\nu$ satisfies the relation $\nu(e^{i\varphi}E_c, n, \varepsilon) = e^{i\varphi}\nu(E_c, n, \varepsilon)$ for all $\varphi \in [0, 2\pi)$.*

This theorem is based on the general results in [6], [7], [8], [33]. We observe that the term $\nu(E_c, n, \varepsilon)$ enters $E_X$ with a factor $\varepsilon$ in front. Hence, $\nu$ enters system (2.8) with a factor of order $O(\varepsilon^2)$. Consequently, the replacement of $\nu$ by 0 is a regular perturbation of (2.8) preserving the rotational symmetry of (2.8). The approximate system is called *mode approximation* and reads

$$\begin{aligned} \frac{d}{dt}E_c &= H_c(n)E_c + \varepsilon a(E_c, n)E_c, \\ \frac{d}{dt}n &= \varepsilon F_0(E_c, n), \end{aligned} \tag{2.9}$$

where

$$\begin{aligned} H_c(n) &= B(n)^{-1}H(n)P_c(n)B(n), \\ a(E_c, n) &= -B(n)^{-1}P_c(n)\partial_n B(n)F_0(E_c, n), \\ F_0(E_c, n, ) &= f(n) - g(n)\left[B(n)E_c, B(n)E_c\right]. \end{aligned}$$

The matrix $H_c(n)$ is a representation of $H(n)$ restricted to its critical subspace $X_c(n)$ in some basis $B(n)$. The matrix $H_c$ depends on the particular choice of $B(n)$, but its spectrum coincides with the critical spectrum of $H(n)$. The term $\varepsilon a E_c$ appears since the space $X_c$ depends on time $t$. Any normally hyperbolic invariant manifold (e.g., fixed point, periodic orbit, invariant torus) that is present in the dynamics of (2.9) persists under the perturbation $O(\varepsilon^2)\nu$. Hence it is also present in system (2.8), describing the flow on the invariant manifold $\mathcal{C}$, and in the semiflow of the complete system (1.1). Furthermore, its hyperbolicity and the exponential attraction toward $\mathcal{C}$ ensure its continuous dependence on small parameter perturbations.

*Remark.* System (2.9) still depends on $\varepsilon$. Hence we should investigate how the transversal Lyapunov exponents depend on $\varepsilon$ for any normally hyperbolic invariant manifold found in the subsequent analysis of (2.9). It was pointed out in [32] that system (2.9) is conservative for

**Table 1**

*Choice of parameters for the bifurcation diagrams presented in sections 3 and 4.*

| | | | |
|---|---|---|---|
| $l_1 = 1$ | $l_2 = 1.136$ | $r_0 = 10^{-5}$ | $r_L = \eta e^{2\pi i\varphi}$ |
| $\beta_1^0 = -0.275$ | $\beta_2^0 = 0$ | $\kappa_1 = 3.96$ | $\kappa_2 = 0$ |
| $g_1 = 2.145$ | $g_2 = \rho_2 = 0$ | $\alpha_1 = 5$ | $\rho_1 = 0.44$ |
| $\Gamma_1 = 90$ | $\Omega_{r,1} = -20$ | $I = 6.757 \cdot 10^{-3}$ | $\tau = 3.59 \cdot 10^2$ |

$q = 1$ at $\varepsilon = 0$. Thus we must expect that the normal hyperbolicity of most objects is of order $o(1)$ for $\varepsilon \to 0$.

However, we will perform the bifurcation analysis for (2.9) only for one fixed "physically realistic" $\varepsilon$, checking the eigenvalues of relative equilibria and the Floquet multipliers of modulated waves numerically.

**2.3. Particular choice of parameters.** The mode approximations (2.9) derived in section 2.2 permit detailed studies of their long-time behavior since they are low-dimensional ODEs. The particular form of system (2.9) depends on the number $q$ of critical eigenvalues on the imaginary axis at the threshold $n_0$. We restrict our interest to cases where the number $q$ of critical eigenvalues of $H$ is at most 2.

Furthermore, we adjust the relative resonance frequency of the material, $\Omega_{r,1}$, in the following manner: The solitary section $S_1$ with zero facet reflectivities, gain dispersion, and feedback, i.e., $\rho_1 = r_0 = r_L = 0$, is symmetric with respect to reflection. Thus, if $H(n)$ has the eigenvalue $\lambda + i \operatorname{Im} \beta_1(n)$, it also has the eigenvalue $\bar{\lambda} + i \operatorname{Im} \beta_1(n)$. Typically, a pair of eigenvalues becomes critical having the frequencies $\operatorname{Im} \lambda_{1,2} \approx \operatorname{Im} \beta_1(n_0) \pm \kappa_1$. The frequency region $(\operatorname{Im} \beta_1 - \kappa_1, \operatorname{Im} \beta_1 + \kappa_1)$ is usually referred to as the *stopband* of the active section. Hence the solitary section $S_1$ can have *on-states* (i.e., rotating-wave solutions, relative equilibria of (1.1)) at both ends of the stopband. We break the reflection symmetry by choosing $\rho_1 > 0$ and $\Omega_{r,1}$ outside of the stopband frequency region. Then the slope of the gain curve (see the appendix) favors frequencies closer to $\Omega_{r,1}$ such that the solitary active section $S_1$ has a distinct stable on-state at the threshold $n_0$.

We choose the feedback phase and strength as our primary bifurcation parameters and use numerical continuation methods [11] to explore the bifurcation diagram in the two-parameter plane keeping all other parameters fixed according to Table 1. We can do so by varying the absolute value $\eta$ and the phase $\varphi$ of $r_L := \eta e^{2\pi i\varphi}$, setting $\beta_2 = 0$ without loss of generality. This is in contrast to the experiments, where $\beta_2$ is varied by changing the current in the feedback section, but $r_L$ is kept fixed. Hence the experimenters cannot vary the parameters $\varphi$ and $\eta$ independently in a continuous manner.

In order to obtain the coefficients of (2.9), we have to compute the critical eigenvalues, their corresponding eigenvectors, and the adjoint eigenvectors.

The critical eigenvalues are roots of the characteristic function $h$ of $H(n)$ defined in Lemma 2.3. We include $n$, $\eta$, and $\varphi$ as parameters to emphasize that the eigenvalue $\lambda_j$ depends on them (see section 2.2):

$$0 = h(\lambda_j, n, \eta, \varphi) = (\eta e^{2\pi i\varphi - 2\lambda_j l_2}, -1) T_1(1; \lambda_j, n) \begin{pmatrix} r_0 \\ 1 \end{pmatrix}.$$

The eigenvector $v_j = (\psi_j, p_j)$ corresponding to $\lambda_j$ and its adjoint $v_j^\dagger = (\psi_j^\dagger, p_j^\dagger)$ are defined up to a scaling by (see [3], [34] for the adjoint)

$$\begin{pmatrix}\psi_j\\ p_j\end{pmatrix} = \begin{pmatrix} T(z,0;\lambda_j,n)\begin{pmatrix}r_0\\1\end{pmatrix},\\ \frac{\Gamma}{\lambda_j - i\Omega_r + \Gamma} T(z,0;\lambda_j,n)\begin{pmatrix}r_0\\1\end{pmatrix}\end{pmatrix}, \qquad \begin{pmatrix}\psi_j^\dagger\\ p_j^\dagger\end{pmatrix} = \begin{pmatrix}\begin{pmatrix}\bar\psi_{j,2}\\ \bar\psi_{j,1}\end{pmatrix}\\ \frac{\rho}{\Gamma}\begin{pmatrix}\bar p_{j,2}\\ \bar p_{j,1}\end{pmatrix}\end{pmatrix}. \tag{2.10}$$

In (2.10), $T(z,0;\lambda_j,n) = T_1(z;\lambda_j,n)$ if $z \le 1$, and

$$T(z,0;\lambda_j,n) = \begin{pmatrix} e^{-\lambda_j z} & 0\\ 0 & e^{\lambda_j z}\end{pmatrix} T_1(1;\lambda_j,n) \quad \text{if } z \ge 1.$$

## 3. The single-mode case.

**3.1. Definition of the system.** First, we consider the generic case, where a single eigenvalue $\lambda$ of $H(n)$ is on the imaginary axis ($q = 1$) at $n = n_0$. Since we have chosen the configuration of the active section $S_1$ such that it has only one stable on-state at $\eta = 0$, this model is certainly valid for sufficiently small $\eta$ in the vicinity of $n_0$. Since $\lambda$ is uniformly isolated, it depends smoothly on $n$ and all parameters. The basis $B(n)$ is the eigenvector $v = (\psi, p)$ associated to $\lambda$, and the projection $B(n)^{-1}P_c(n)$ is the corresponding adjoint eigenvector $v^\dagger$. The term $a$ in (2.9) vanishes if we scale $v$ and $v^\dagger$ such that $\langle v, v^\dagger\rangle = 1$ for all $n$ under consideration. Moreover, we can decouple the phase of the complex quantity $E_c$ in (2.9) due to the rotational symmetry of the system. Hence we have to analyze a system for $S = |E_c|^2$, $n$, and $\lambda$ which reads as follows:

$$\dot S = 2\,\mathrm{Re}(\lambda) S, \tag{3.1}$$

$$\dot n = \varepsilon\,(I_1 - n - R(\lambda, n, \varphi, \eta)S)\,, \tag{3.2}$$

$$0 = \ h(\lambda, n, \varphi, \eta), \tag{3.3}$$

where $\varepsilon = \tau^{-1}$, $I_1 = I\tau$, and the coefficient $R$ is defined as follows:

$$R(\lambda, n, \varphi, \eta) = [G(n) - \rho_1 + \mathrm{Re}\,\chi_1(\lambda)](\psi, \psi)_1^2$$

(see the appendix for the definition of $\chi$).

On-states are equilibria of (3.1)–(3.3), whereas periodic solutions of (3.1)–(3.3) represent quasi-periodic solutions of (2.9). This type of modulated rotating-wave solution is typically referred to as *self-pulsation*. Several analytic and computational results have been obtained previously about the existence regions of self-pulsations and their synchronization properties using the single-mode approximation [2], [3], [5], [31], [34].

System (3.1)–(3.3) is a differential-algebraic equation (DAE). Its inherent dynamical system is two-dimensional. Standard numerical continuation software such as, e.g., AUTO [11] is not able to treat DAEs directly. However, we can easily convert (3.1)–(3.3) to an equivalent explicit system of ODEs by changing (3.3) to

$$\dot\lambda = -\frac{\partial_n h(\lambda, n, \varphi, \eta)\dot n + c \cdot h(\lambda, n, \varphi, \eta)}{\partial_\lambda h(\lambda, n, \varphi, \eta)} \tag{3.4}$$

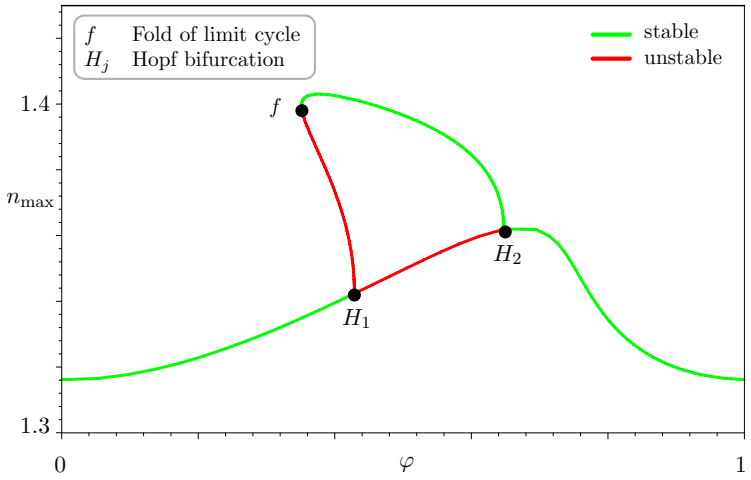


**Figure 2.** *Bifurcation diagram for $\eta = 0.1$. We report the n-component for the on-state and the maximum of the n-component for the periodic solutions.*

if $\lambda$ is an isolated simple root of $h$. For sufficiently large $c > 0$, (3.1), (3.2), and (3.4) is a four-dimensional ODE which has a stable invariant manifold defined by $h = 0$. On this invariant manifold, the flow is identical to the flow of (3.1)–(3.3). The transformation of (3.3) to (3.4) is sometimes referred to as Baumgarte regularization [10].

*Remark.* There should exist a curve $md$ in the parameter plane $(\varphi, \eta)$ which bounds the range of validity of the single-mode model in the following sense: the function $\lambda(n)$ defined implicitly by (3.3) has a discontinuous derivative $\partial_n \lambda(n)$ along some line $n = n_{md}$ in the phase plane for $(\varphi, \eta) \in md$, i.e., $\partial_\lambda h(\lambda(n), n, \varphi, \eta) = 0$ ($\lambda$ is a double root of $h$). Hence we expect the continuation of families of periodic orbits or equilibria to fail if it crosses the curve $md$.

**3.2. The bifurcation diagram.** We explore the dynamics numerically in the two-parameter plane $(\varphi, \eta)$, choosing the other parameters according to the example presented in [35] (see Table 1). The procedure is as follows: First, we choose a very small feedback level $\eta = 0.1$ and report the smallest $n_0$ such that $H(n_0)$ possesses an eigenvalue on the imaginary axis for $\varphi = 0$, i.e., $h(\cdot, n_0, 0, \eta)$ has a purely imaginary root. This is $n_0 = 1.316194$ for the parameter situation outlined in Table 1. The corresponding root of $h$ is $\lambda = -1.632607i$. We consider only this eigenvalue $\lambda$ of $H$ and its eigenvector $\psi$ in (3.3) in this section. There exists an equilibrium with $S = (I_1 - n_0)/R(\lambda, n_0, 0, \eta)$ and $n = n_0$. In the next step, we report on how this equilibrium changes its location in phase space and its stability under variation of $\varphi$ (see Figure 2). Note that the location of the equilibrium coincides exactly with the location of the corresponding rotating-wave solution of the complete system (1.1).

Adding $\eta$ as a free parameter, we compute the curve of Hopf points and the curve of saddle-nodes (folds) of limit cycles in the two-parameter plane $(\varphi, \eta)$ (see the full bifurcation diagram Figure 4). The saddle-node curve of limit cycles and the Hopf curve meet at a stable generalized Hopf point $GH_1$ [14]. Both ends of the Hopf curve meet at the point $MD = (\varphi_0, \eta_0)$. The point $MD$ is situated on the curve $md$. Moreover, the equilibrium of system (3.1)–(3.3) is situated on the line $n = n_{md}$ for the parameters $(\varphi_0, \eta_0)$. We refer to it

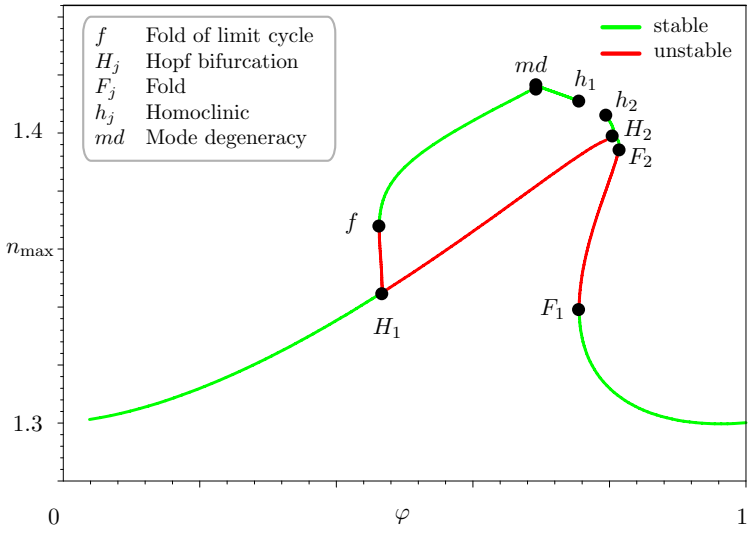


**Figure 3.** *Bifurcation diagram at $\eta = 0.2$. We report the n-component for the on-state and the maximum of the n-component for the periodic solutions. The family of periodic orbits is discontinuous at md.*

as an equilibrium with *mode degeneracy* as $\lambda$ is an eigenvalue of $H(n)$ of algebraic multiplicity 2. We explore the vicinity of this equilibrium using the two-mode approximation in section 4 since the number $q$ of critical eigenvalues of $H(n)$ is 2 near $MD$.

Starting from one of the Hopf points at $\eta = 0.2$, we draw another one-dimensional bifurcation diagram, keeping $\eta = 0.2$ fixed but varying $\varphi$. The numerical result is shown in Figure 3.

The line of equilibria has folded twice at $F_1$ and $F_2$ in saddle-node bifurcations. The family of periodic orbits starting from $H_2$ is stable and ends in a homoclinic bifurcation at $h_2$. The family of periodic orbits starting from $H_1$ is unstable and collides with a stable branch in the saddle-node bifurcation of limit cycles $f$. Continuing the stable branch of periodic solutions starting from $f$, we approach a discontinuity of system (3.1)–(3.3) at $md$. Hence there is no *continuous* family of periodic orbits between $h_1$ and $f$.

In the last step, we continue the saddle-node points $F_1$ and $F_3$ and the homoclinic orbit[1] $h_2$, varying both parameters, $\eta$ and $\varphi$. Figure 4 shows the complete two-parameter bifurcation diagram, and Figure 5 shows the corresponding symbolic phase portrait sketches. We note that the two saddle-node bifurcations observed in Figure 3 emanate from a cusp bifurcation at $CU$ in Figure 4. Moreover, the curve of homoclinic bifurcations in the $(\varphi, \eta)$-plane starting from $h_2$ at $\eta = 0.2$ turns back to $\eta = 0.2$ at $h_1$ (see Figure 3). Along this curve, the approach of the homoclinic orbit toward the saddle changes (see Figure 5): There is a parameter path of central saddle-nodes on closed orbits between two noncentral saddle-nodes on closed orbits ($NC_1$–$NC_2$). The region 6 in the vicinity of the central saddle-node on a closed orbit is a classical excitability scenario [15].

*Remark.* The approximation of homoclinic orbits by periodic orbits of large periods is

[1]Actually, we continued periodic orbits of a fixed large period.

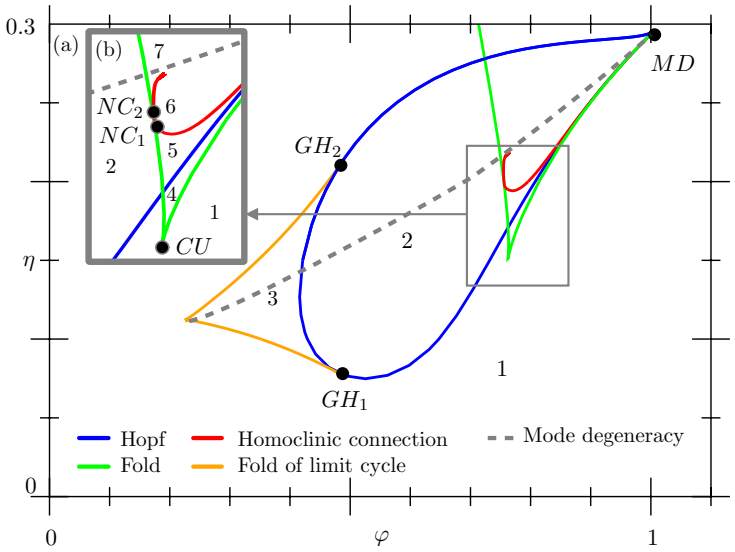


**Figure 4.** *Bifurcation diagram in the two-parameter plane $(\varphi, \eta)$. Codimension 2 bifurcations are marked by black points and labels. GH refers to a generalized Hopf bifurcation, CU to a cusp bifurcation, and NC to a noncentral saddle-node on a closed orbit. MD is an equilibrium where $\partial_\lambda h = 0$ in (3.4). The family of periodic orbits is discontinuous along the dashed line because $\partial_\lambda h(\lambda, n)$ becomes zero on the periodic orbits.*

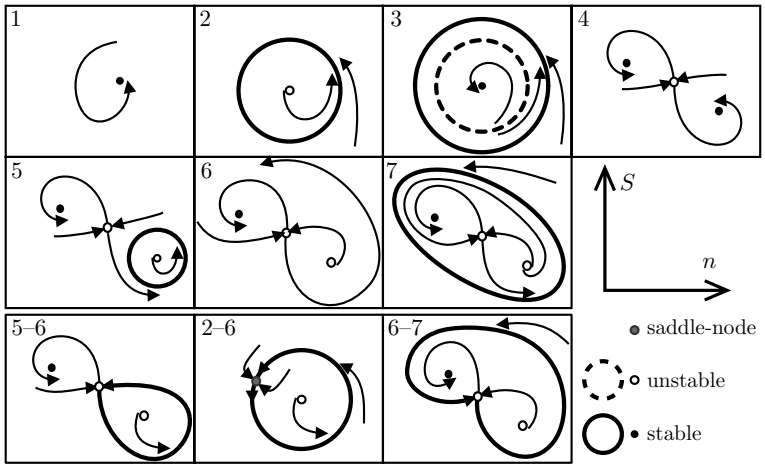


**Figure 5.** *Symbolic phase-portrait sketches for the regions 1 to 7 of Figure 4. In addition, we display the global bifurcations between the regions 2, 5, 6, and 7. Black points symbolize stable equilibria, and white points are unstable equilibria. If an unstable equilibrium is a saddle, we sketch the stable and unstable manifolds. The additional arrows show the behavior of the vector field. The $S - n$ coordinate cross gives a rough orientation.*

very accurate if the equilibrium is a saddle with eigenvalues distant from the imaginary axis. However, the order of approximation is worse in the vicinity of homoclinics to saddle-nodes. For this reason, we have used the HOMCONT part of AUTO to compute the points $NC_1$ and $NC_2$. HOMCONT utilizes projection boundary conditions to approximate the homoclinic

orbit [9], [11].

The continuation of the curve of homoclinic bifurcations in the plane $(\varphi, \eta)$ ends at some distance after (above) the point $NC_2$ in Figure 4, where the homoclinic orbit approaches a point in the phase plane where $\lambda$ is degenerate.

The curve of homoclinic bifurcations, the Hopf curve, and the saddle-node curve in Figure 4 approach each other and become tangent at $MD$. However, this does not imply the presence of a Takens–Bogdanov bifurcation since the model is discontinuous in the vicinity of $MD$. Indeed, the Hopf frequency along the Hopf curve increases toward $MD$.

*Remark.* Figure 5 assumes completeness of the bifurcation diagram Figure 4. The problem of completeness of Figure 4 is not investigated here. There may be additional nested pairs of stable and unstable limit cycles. See, e.g., [21], [32] for a treatment of the single-mode laser as a perturbation of a conservative oscillator of order $O(\sqrt{\varepsilon})$. In [25], a result about the uniqueness of the stable limit cycle is obtained by imposing conditions on the shape of the coefficients $\lambda$ and $R$ in system (3.1), (3.2).

## 4. The two-mode case—unfolding of the mode degeneracy in the parameters $\varphi$ and $\eta$.

**4.1. Definition of $B(n)$ and $P_c(n)$—elimination of the absolute phase.** In this section, we explore in detail the neighborhood of $MD$ from Figure 4, completing the bifurcation diagram for larger feedback levels $\eta$. Let $n_0$ be a threshold carrier density, where $H(n_0)$ has a dominating eigenvalue $\lambda$ of algebraic multiplicity 2 on the imaginary axis. An $n_0$ of this type exists, e.g, in the point $MD = (\varphi_0, \eta_0)$ of the parameter plane $(\varphi, \eta)$ (see Figure 4). Hence the complex dimension $q$ of the critical subspace $X_c$ is 2, and the real dimension of the invariant manifold $\mathcal{C}$ is 5 (see section 2.2). In order to obtain the coefficients of system (2.9), we have to construct a basis $B(n)$ and a projector $P_c(n)$ which depend smoothly on $n$, and the bifurcation parameters $\eta$ and $\varphi$ in the vicinity of $n_0$, $\varphi_0$, and $\eta_0$.

Let $\lambda_1$ and $\lambda_2$ be the two roots of $h(\cdot, n, \varphi, \eta)$ which coincide and are situated on the imaginary axis if $n = n_0$, $\varphi = \varphi_0$, and $\eta = \eta_0$. We denote the corresponding eigenvectors $(\psi_j, p_j)$ by $v_j$ and the adjoint eigenvectors by $v_j^\dagger$ $(j = 1, 2)$. The vectors $v_j$ and $v_j^\dagger$ are defined in (2.10). Hence $v_j$ and $v_j^\dagger$ depend analytically on $\lambda_j$.

We introduce the quantities

$$\theta := \frac{1}{2}(\lambda_1 + \lambda_2), \qquad \mu := \frac{1}{4}(\lambda_1 - \lambda_2)^2$$

and define the basis $B = [u_1, u_2]$ by

$$u_1 = \frac{v_1 - v_2}{\lambda_1 - \lambda_2}, \qquad u_2 = \frac{1}{2}(v_1 + v_2). \tag{4.1}$$

$\theta$ and $\mu$ depend smoothly on $n$, $\varphi$, and $\eta$ in the vicinity of the degeneracy $MD$. The vectors $u_1$ and $u_2$ do not change if we permute the eigenvalues $\lambda_1$ and $\lambda_2$. Moreover, they are smooth with respect to $n$, $\varphi$, and $\eta$ and uniformly linearly independent around the degeneracy point. We denote the $\psi$-component of $u_j$ by $\xi_j$ $(j = 1, 2)$. The representation of $H$ in the basis $B$ reads

$$Hu_1 = \theta u_1 + u_2, \qquad Hu_2 = \mu u_1 + \theta u_2. \tag{4.2}$$

Hence the representation of $H$ with respect to the basis $B$ is smooth in the degeneracy point.

Furthermore, we define the following functionals for $x \in \mathbb{L}^2([0,L];\mathbb{C}^4)$ and $y \in \mathbb{L}^2([0,L];\mathbb{C}^2)$:

$$\begin{aligned} P_1 x &= \frac{1}{2}\left[\frac{\lambda_1-\lambda_2}{(v_1^\dagger,v_1)}(v_1^\dagger,x)+\frac{\lambda_2-\lambda_1}{(v_2^\dagger,v_2)}(v_2^\dagger,x)\right], & P_2 x &= \frac{(v_1^\dagger,x)}{(v_1^\dagger,v_1)}+\frac{(v_2^\dagger,x)}{(v_2^\dagger,v_2)},\\ \Theta_1 y &= (G(n)-\rho_1+\chi_1(\lambda_1))(\psi_1,y)_1, & \Theta_2 y &= (G(n)-\rho_1+\chi_1(\lambda_2))(\psi_2,y)_1,\\ Q_1 y &= \frac{\Theta_1 y-\Theta_2 y}{\bar\lambda_1-\bar\lambda_2}, & Q_2 y &= \frac{1}{2}\left(\Theta_1 y+\Theta_2 y\right). \end{aligned}$$

(See the appendix for the definition of $\chi_1$.) $P_1$ and $P_2$, as well as $Q_1$ and $Q_2$, are not affected by a permutation of $\lambda_1$ and $\lambda_2$. Since $P_j u_k = \delta_{jk}$, the functionals $P_j$ depend smoothly on $n$ and are uniformly linearly independent around the degeneracy. We define

$$P_c x = [P_1 x]u_1 + [P_2 x]u_2.$$

Using these definitions of $B$ and $P_c$, system (2.9) reads as follows ($E_c = (x_1,x_2) \in \mathbb{C}^2$):

$$\begin{aligned} \dot x_1 &= \theta(n)x_1 + \mu(n)x_2 - \dot n(P_1(n)\partial_n u_1(n)x_1 + P_1(n)\partial_n u_2(n)x_2),\\ \dot x_2 &= x_1 + \theta(n)x_2 - \dot n(P_2(n)\partial_n u_1(n)x_1 + P_2(n)\partial_n u_2(n)x_2),\\ \dot n &= \varepsilon\left[I_1 - n - \operatorname{Re}\left(|x_1|^2 Q_1\xi_1 + |x_2|^2 Q_2\xi_2 + \bar x_1 x_2 Q_1\xi_2 + \bar x_2 x_1 Q_2\xi_1\right)\right]. \end{aligned} \tag{4.3}$$

Finally, we observe that we can eliminate the absolute phase of the vector $(x_1,x_2)$ due to the rotational symmetry of system (4.3). We introduce the quantities

$$r = |x_1|^2 - |x_2|^2 \qquad (r\in\mathbb{R}), \qquad\qquad \zeta = \bar x_1 x_2 \qquad (\zeta\in\mathbb{C}).$$

Using $r$ and $\zeta$, we can recover the quantities

$$|x_1|^2 = \frac{1}{2}(\sqrt{r^2+4|\zeta|^2}+r), \qquad\qquad |x_2|^2 = \frac{1}{2}(\sqrt{r^2+4|\zeta|^2}-r).$$

Hence system (4.3) has a four-dimensional subsystem for $r$, $\zeta$, and $n$ which reads as follows:

$$\begin{aligned} \dot r &= 2\operatorname{Re}\left(b_{11}|x_1|^2 - b_{22}|x_2|^2 + (b_{12}-\bar b_{21})\zeta\right),\\ \dot\zeta &= b_{21}|x_1|^2 + \bar b_{12}|x_2|^2 + (\bar b_{11}+b_{22})\zeta,\\ \dot n &= \varepsilon\left[I_1 - n - \operatorname{Re}\left(|x_1|^2 Q_1\xi_1 + |x_2|^2 Q_2\xi_2 + \zeta Q_1\xi_2 + \bar\zeta Q_2\xi_1\right)\right], \end{aligned} \tag{4.4}$$

where the functions $b_{ij}(r,\zeta,n)$ are defined as

$$\begin{aligned} b_{11}(r,\zeta,n) &= \theta(n) - \dot n P_1(n)\partial_n u_1(n), & b_{12}(r,\zeta,n) &= \mu(n) - \dot n P_1(n)\partial_n u_2(n),\\ b_{21}(r,\zeta,n) &= 1 - \dot n P_2(n)\partial_n u_1(n), & b_{22}(r,\zeta,n) &= \theta(n) - \dot n P_2(n)\partial_n u_2(n). \end{aligned}$$

The quantities $P_i\partial_n u_j$ depend on $n$, $\mu$, and $\theta$ and can be computed by the chain rule:

$$P_i\partial_n u_j = P_i(\partial_n\theta\partial_\theta + \partial_n\mu\partial_\mu + \partial_n)u_j.$$

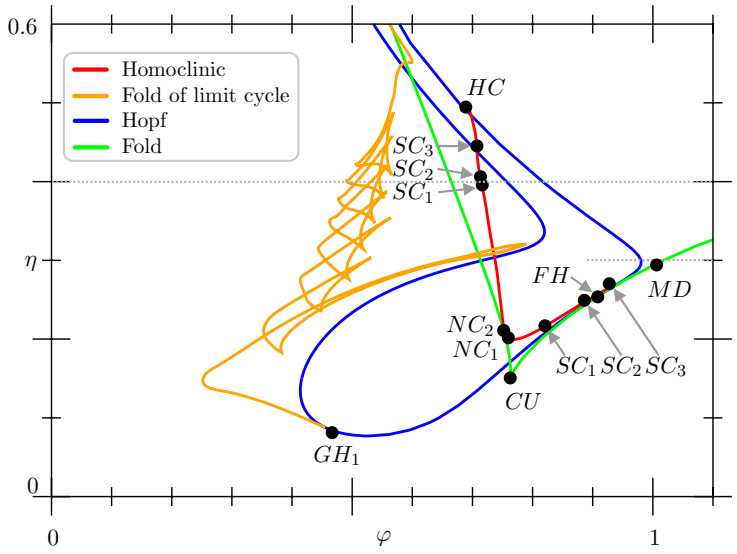


**Figure 6.** *Bifurcation curves of Figure 4 recomputed in the $(\varphi,\eta)$-plane using model (4.4), (4.5). The one-dimensional bifurcation diagrams of Figures 8 and 9 have been obtained along the horizontal dotted lines. This diagram should be compared to Figure 4. Along the curve of homoclinic bifurcations, the points $SC_j$ mark changes of saddle quantities. $FH$ marks a fold-Hopf interaction (see text and Figure 7).*

The functions $\theta(n)$ and $\mu(n)$ are given only implicitly by the root curves of $h(\cdot,n)$. We introduce $\theta$ and $\mu$ as new variables satisfying the differential equations

$$\dot\theta = \frac{1}{2}(\dot\lambda_1+\dot\lambda_2), \qquad \dot\mu = \frac{1}{2}(\dot\lambda_1-\dot\lambda_2)(\lambda_1-\lambda_2) \tag{4.5}$$

in order to put the system in a form that is recognized by AUTO. In (4.5), the equations for $\dot\lambda_j$ are constructed in the same manner as in (3.4). Assembling (4.4) and (4.5), we obtain a system of dimension 8, where all coefficients depend smoothly on $n$, $\varphi$, and $\eta$. This system has a four-dimensional uniformly attracting invariant manifold, where $\theta=\theta(n)$ and $\mu=\mu(n)$. We restrict our bifurcation analysis to this invariant manifold.

**4.2. The bifurcation diagram 2.** We explore the $(\varphi,\eta)$-plane in the same manner as in section 3. First, we redraw the curves of the single-mode bifurcation diagram Figure 4 in the plane $(\varphi,\eta)$ in Figure 6. We observe that the curves are in good quantitative agreement for smaller $\eta$. The curve of the folds even coincides exactly. Notable differences are as follows.

1. The curve of the folds of limit cycles does not connect to the Hopf curve in a generalized Hopf point $GH_2$ in Figure 6, but it turns toward larger $\eta$ undergoing a sequence of cusps.

2. In Figure 6, the Hopf curve and the fold curve meet each other in $FH$ in a fold-Hopf interaction of type "$s=1,\theta<0$" according to [16]. A small neighborhood of $FH$ in parameter space is depicted in Figure 7. The time must be reversed compared to [16] since the torus bifurcation in Figure 7 is supercritical. We observe that the equilibrium with mode degeneracy is no longer a special point except that it is situated on the fold curve.

The curve of homoclinic bifurcations depicted in the single-mode bifurcation diagram Figure 4 can be continued in both directions for increasing $\eta$. However, the characteristic

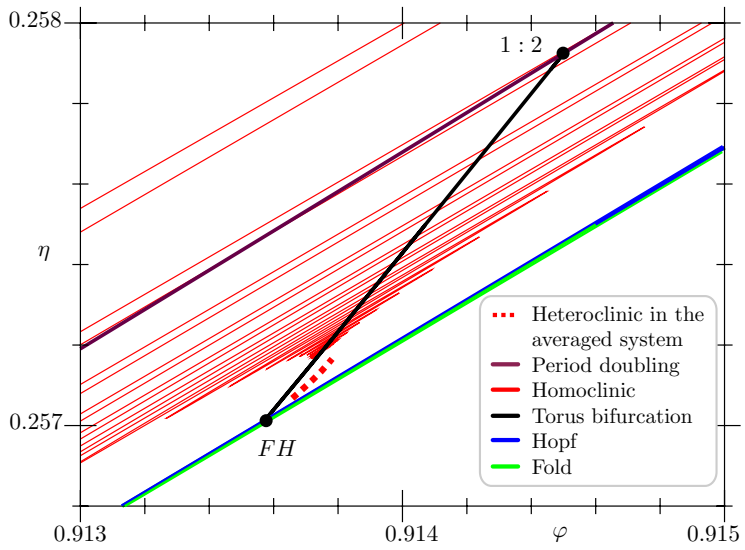


**Figure 7.** *Local (incomplete) bifurcation diagram in the vicinity of the fold-Hopf interaction $FH$ in the $(\varphi, \eta)$-plane. There is a $1:2$ resonance at the point $1:2$. The dotted line has not been actually computed. It is inserted in the picture to simplify the identification of the appropriate fold-Hopf interaction type in, e.g.,* [16].

quantities of the linearized system at the saddle change along the line (see Figure 6): At $SC_1$, we have three leading stable eigenvalues. For higher $\eta$, a complex pair of eigenvalues becomes dominant in the negative half-plane, turning the homoclinic orbit into a saddle-focus homoclinic connection. Denote the real part of this complex pair of eigenvalues by $\sigma_s$ and the real part of the (real) unstable eigenvalue by $\sigma_u$. Between $SC_1$ and $SC_2$, we have $\nu := -\sigma_u/\sigma_s < 1$.

At $SC_2$, the saddle becomes neutral, i.e., $\nu = 1$, and, at $SC_3$, we have $\nu = 2$. Shilnikov's theorems [16] imply that there is one stable limit cycle in the vicinity of the homoclinic bifurcation before $SC_2$, i.e., along $NC_1$–$SC_2$ and $NC_2$–$SC_2$, but there are infinitely many limit cycles in the vicinity of the homoclinic bifurcation after $SC_2$. Furthermore, infinitely many of these limit cycles are stable between $SC_2$ and $SC_3$. We observe that one end of the curve of homoclinic bifurcations approaches the fold-Hopf interaction $FH$ in an oscillatory manner (see the curve of homoclinic bifurcations in Figure 7).

We must reach the upper end $HC$ of the curve of homoclinic bifurcations (see Figure 6) before the saddle having the homoclinic connection undergoes a subcritical Hopf bifurcation. At the point $HC$, there is a heteroclinic connection between the saddle and the small Hopf cycle which is also of saddle type (two unstable and one stable Floquet multipliers).

Figure 6 gives a complete overview concerning the equilibria of system (4.4), (4.5), i.e., their number, the number of their stable and unstable directions, and their local bifurcations. In order to get more information about the periodic orbits and global bifurcations, we draw one-dimensional bifurcation diagrams varying $\varphi$ at $\eta = 0.3$ (see Figure 8) and $\eta = 0.4$ (see Figure 9 (a)) by continuing the periodic orbits from the Hopf bifurcations.

In Figure 8, we observe that the family of periodic orbits emerging at the saddle Hopf point undergoes a sequence of folds and period doublings approaching a homoclinic connection to a

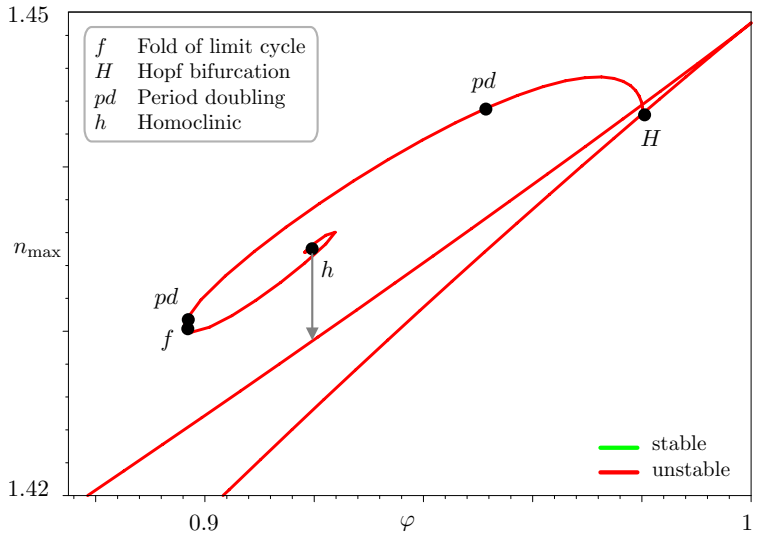


**Figure 8.** *Bifurcation diagram for $\eta = 0.3$ for a part of the full phase period for $\varphi$. We report the $n$-component for the on-state and the maximum of the $n$-component for the periodic solutions. The arrow points to the saddle approached by the homoclinic $h$. This saddle is of focus-focus type. Only the first period doublings and folds are reported.*

focus-focus. Parts of the family are stable according to Shilnikov's theorems [16] because the linearization at the focus-focus has a negative saddle value; i.e., the real part of the unstable eigenvalues is smaller than the modulus of the real part of the stable eigenvalues.

In Figure 9 (a), the two Hopf points are connected by a "small bridge" of periodic solutions undergoing a torus bifurcation at $t$. We observe that both Hopf points are close to the point $X$, where the saddle equilibrium and the former node equilibrium have equal $n$-component. At $X$, there are two eigenvalues of $H(n)$ with different imaginary parts on the imaginary axis in the equilibria. The periodic orbits between $H_1$ and $H_2$ have an angular velocity corresponding approximately to the difference between these two eigenvalues. Typically, this type of self-pulsation is called mode beating or mixed-mode self-pulsation; see [13] and references therein. These oscillations are of great interest because their frequency can be of order $O(1)$ in our scaling. In our case, the angular velocity of the oscillations increases from 0.2 for $\eta = 0.2$ to 0.4 for $\eta = 0.6$ along the channel between the two Hopf curves in Figure 6 which corresponds to frequencies between 11 and 22 GHz.

The family of periodic orbits emerging from the homoclinic bifurcation (the red curve of Figure 6) is now disconnected from the family of equilibria. It folds several times and approaches a transversal homoclinic intersection of a periodic orbit. We have depicted this end of the family enlarged in Figure 9 (b) and (c). Figure 9 (d) displays how a typical periodic orbit close to the homoclinic intersection looks.

Adding $\eta$ as a free parameter, we continue the homoclinic bifurcations, the first period doublings and folds of limit cycles of Figure 8, and the torus bifurcation of Figure 9 in two parameters. The resulting bifurcation curves are depicted in Figure 10. We observe the following.

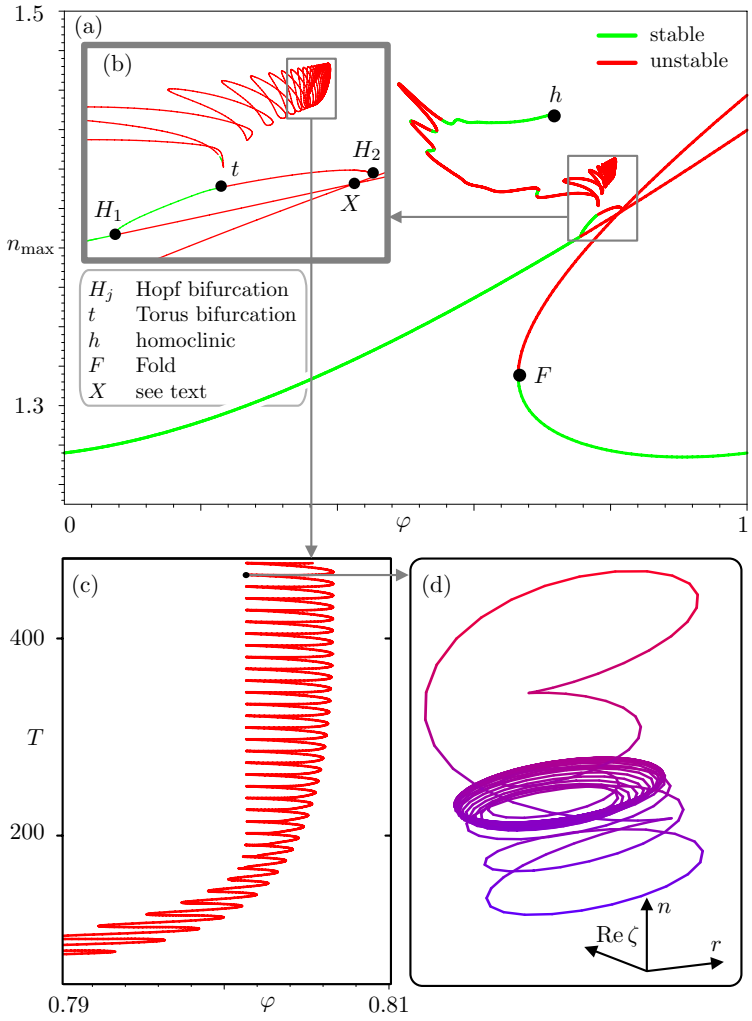


**Figure 9.** *Bifurcation diagram for $\eta = 0.4$. Diagram* (b) *shows the framed region enlarged. In* (a) *and* (b)*, we report the n-component for the on-state and the maximum of the n-component for the periodic solutions. In* (c)*, we report the period for the family approaching a transversal homoclinic intersection.* (d) *shows a projection of the phase portrait of one of the periodic orbits.*

1. The curve of homoclinic bifurcations forms a closed loop. The stable eigenvalues become real for smaller $\eta$: There are focus-focus to saddle-focus transitions at $SC_1$ and $SC_2$ in Figure 10. However, the saddle value is negative along the whole loop. Hence there are infinitely many stable periodic orbits in the vicinity of the loop of homoclinics.

2. The curve of period doublings forms a closed loop. It meets the torus bifurcation curve starting from the fold-Hopf interaction $FH$ and the torus bifurcation curve passing $t$ in Figure 9 in $1:2$ resonances (see Figures 7 and 10). There are infinitely many other period doubling curves in the vicinity of the loop of homoclinics.

3. The curve of folds of limit cycles ends in an unstable generalized Hopf bifurcation [14] at $GH_2$ in one direction. There are infinitely many curves of folds of limit cycles in the

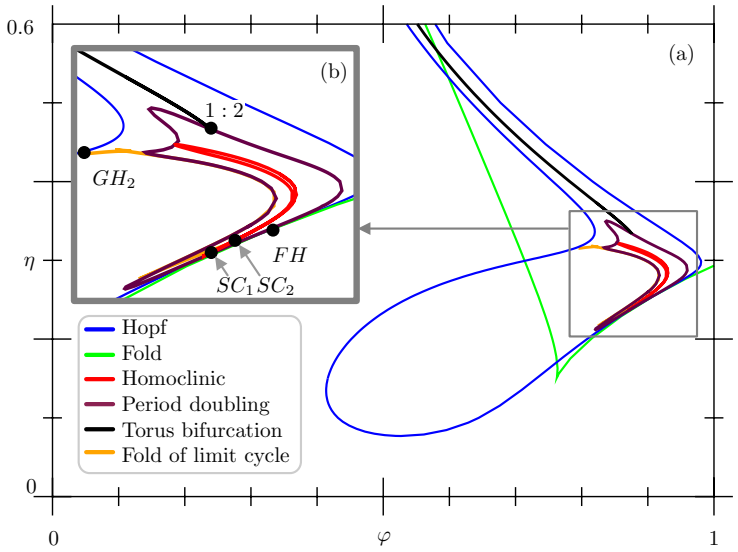


**Figure 10.** *Location of the homoclinic, period doubling, and torus bifurcation. The Hopf curve and the saddle-node curve are also drawn for orientation.* (b) *shows the framed region enlarged. The vicinity of the fold-Hopf interaction $FH$ is shown in Figure 7. The curve of folds of limit cycles is partially obscured by the period doubling curve due to its proximity (see, e.g., Figure 8).*

vicinity of the loop of homoclinic bifurcations.

**5. Conclusions—outlook.** In this paper, we performed a numerical bifurcation analysis for a system of ODEs describing delayed optical feedback phenomena in a semiconductor laser with short cavity. We constructed the model analytically in advance by reducing the traveling-wave model with gain dispersion [4], [25], a singularly perturbed system of PDEs, to a local center manifold [26], [32]. The bifurcation parameters were the phase $\varphi$ and the strength $\eta$ of the delayed optical feedback.

In the first step, we analyzed the single-mode dynamics for small $\eta$, observing Hopf instabilities and two fold curves of the equilibria. The single-mode self-pulsations emerging at the Hopf bifurcation typically have an angular velocity of order $O(\sqrt{\varepsilon})$ or less as they approach a homoclinic bifurcation (see the region bordered by the dashed gray line in Figure 11). A certain part of the homoclinic is actually a closed orbit to a saddle-node, implying excitability [15] in the vicinity of the homoclinic bifurcation (see the yellow region in Figure 11).

In the second step, we extended our analysis to the neighborhood of the mode degeneracy point $MD$ detected in the single-mode analysis using an appropriately posed two-mode system (a system of ODEs of dimension 4). We observed that there is a fold-Hopf interaction close to the point $MD$ in the $(\varphi, \eta)$-plane and that the homoclinic orbits change into saddle-focus connections for larger $\eta$, implying complicated dynamics according to Shilnikov's theorems. Furthermore, we found another type of self-pulsation often referred to as mode beating or mixed-mode self-pulsation [13] (see light gray region in Figure 11). The angular velocity of the mixed-mode oscillations is related to the difference of the imaginary parts of two critical eigenvalues of $H$. Hence it can be of order $O(1)$, which makes this type of oscillation

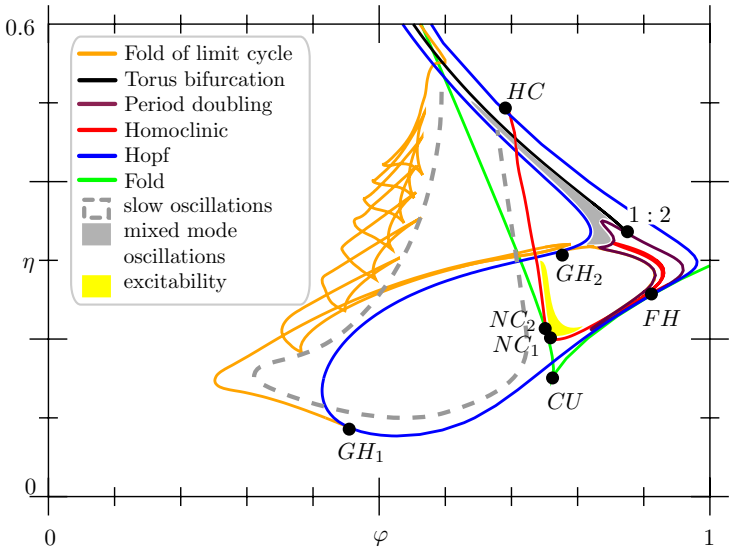


**Figure 11.** *Bifurcation diagram in the (phi, η)-plane—overview. The bifurcations of codimension* 2*, marked by black points and labels, are explained in detail in sections* 3.2 *and* 4.2*. Some regions of interest for practical applications are pointed out in particular.*

particularly interesting for applications.

In addition, we detected a torus bifurcation of the mixed-mode self-pulsations that ends in a strong $1:2$ resonance. The period doubling bifurcation crossing this strong resonance is only the first one in an infinite sequence accumulating to a curve of homoclinic bifurcations of focus-focus type. Again, Shilnikov's theorems imply the existence of stable complicated dynamics in the vicinity of these homoclinic bifurcations. Figure 11 assembles all pictures concerning the $(\varphi, \eta)$-plane.

In summary, the map in the $(\varphi, \eta)$-plane (see Figure 11) shows the roots and borders of many delayed optical feedback phenomena observed experimentally and numerically [24], [35]. The diagram contains points (e.g., the fold-Hopf interaction and the strong resonance) and curves (e.g., homoclinic connections to saddle-foci or foci-foci) which imply the presence of complicated dynamics. Hence the diagram remains incomplete. However, several phenomena of particular practical interest have been detected and precisely located, e.g., single-mode and mixed-mode self-pulsations and excitability.

In the future, we will investigate other interesting experimental configurations (e.g., dispersive feedback, active feedback). Moreover, we will study some of the bifurcations of codimension 2 of Figure 11 in more detail and compare the bifurcation diagrams to simulation results for the complete PDE system (1.1). Moreover, it is interesting to note that first examinations of the Lang–Kobayashi system using the methods outlined in this paper lead to bifurcation diagrams of the same structure. This points to the mode degeneracy of $H(n)$, which is common to both models as the organizing center. Hence it is worth studying the normal form for laser equations close to a mode degeneracy proposed by [32] in detail.

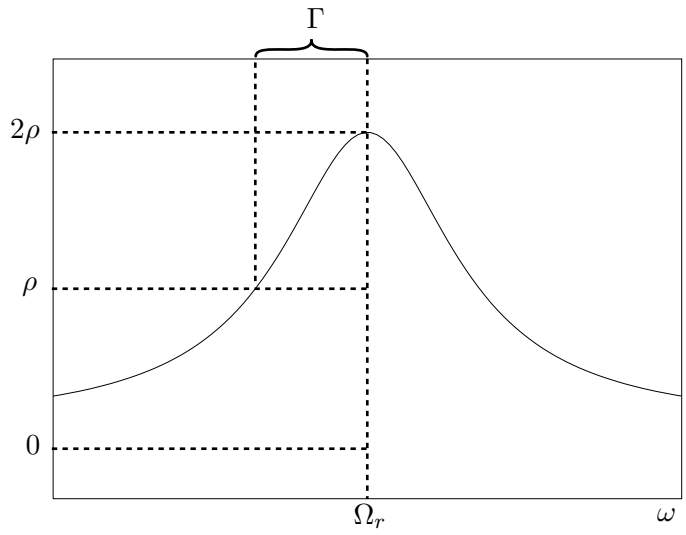


**Figure 12.** *Shape of the Lorentzian* $2\,\mathrm{Re}\,\chi(i\omega)$ *for* $\omega \in \mathbb{R}$ *and visualization of its parameters (see Table 2).*

**6. Appendix. Physical interpretation of the traveling-wave equations—discussion of typical parameter ranges.** System (2.1) is well known as the traveling-wave model describing longitudinal dynamical effects in semiconductor lasers (see [4], [18], [29] for further references). Results of numerical simulations have been presented in [2], [3], [4], [5], [24].

The quantities $\psi$ and $p$ describe the complex optical field $E$ in a spatially modulated waveguide:

$$E(\vec{r},t) = E(x,y)\cdot(\psi_1(t,z)e^{i\omega_0 t - i\frac{\pi}{\Lambda}z} + \psi_2(t,z)e^{i\omega_0 t + i\frac{\pi}{\Lambda}z}).$$

The complex amplitudes $\psi_{1,2}(t,z)$ are the longitudinally slowly varying envelopes of $E$. The transversal space directions are $x$ and $y$, the longitudinal direction is $z$, and $\vec{r} = (x,y,z)$. For periodically modulated waveguides, $\Lambda$ is the longitudinal modulation wavelength. The central frequency is $\omega_0/(2\pi)$, and $E(x,y)$ is the dominant transversal mode of the waveguide.

The equation $\dot{E} = H(n)E$ for an uncoupled waveguide ($\kappa = 0$), a monochromatic light-wave in the forward direction $e^{i\omega t}\psi_1(z)$, and a constant carrier density $n$ imply a spatial shape of the power $|\psi_1|^2$ according to

$$\partial_z|\psi_1(z)|^2 = (2\,\mathrm{Re}\,\beta(z) + 2\,\mathrm{Re}\,\chi(i\omega,z))|\psi_1(z)|^2, \tag{6.1}$$

where

$$\chi(i\omega,z) = \frac{\rho(z)\Gamma(z)}{i\omega - i\Omega_r(z) + \Gamma(z)}. \tag{6.2}$$

$2\,\mathrm{Re}\,\chi(i\omega,z))$ is a Lorentzian intended to fit the gain curve of the waveguide material (see Figure 12). Hence $\dot{E} = HE$ produces gain dispersion; i.e., the spatial growth rate of the wave $e^{i\omega t}\psi(z)$ depends on its frequency $\omega$. The variable $p(t,z)$ reports the internal state of the

**Table 2**

*Ranges and explanations of the variables and coefficients appearing in (2.1)–(2.4). See also [4], [27] to inspect their relations to the originally used physical quantities and scales.*

| | Typical range | Explanation |
|---|---|---|
| $\psi(t,z)$ | $\mathbb{C}^2$ | optical field, forward and backward traveling wave |
| $i \cdot p(t,z)$ | $\mathbb{C}^2$ | nonlinear polarization for the forward and backward traveling wave |
| $n(t)$ | $(\underline{n}, \infty)$ | spatially averaged carrier density in section $S_1$ |
| $\operatorname{Im} \beta_k^0$ | $\mathbb{R}$ | frequency detuning |
| $\operatorname{Re} \beta_k^0$ | $< 0$, $(-10, 0)$ | decay rate due to internal losses |
| $\alpha_H$ | $(0, 10)$ | negative of line-width enhancement factor |
| $g_1$ | $\approx 1$ | differential gain in $S_1$ |
| $\kappa_k$ | $(-10, 10)$ | real coupling coefficients for the optical field $\psi$ |
| $\rho_k$ | $[0, 1)$ | $\rho_k$ is maximum of the gain curve |
| $\Gamma_k$ | $O(10^2)$ | half width of half maximum of the gain curve |
| $\Omega_{r,k}$ | $O(10)$ | resonance frequency |
| $I$ | $O(10^{-2})$ | current injection in section $S_1$ |
| $\tau$ | $O(10^2)$ | spontaneous lifetime for the carriers |
| $P$ | $(0, \infty)$ | scale of $(\psi, p)$ (can be chosen arbitrarily) |
| $r_0$, $r_L$ | $\mathbb{C}$, $\lvert r_0\rvert, \lvert r_L\rvert < 1$ | facet reflectivities |

gain filter. See [4], [27] for more details. The Lorentzian gain filter is also used by [1], [18], and [20]. Since the coefficients $\rho$, $\Gamma$, and $\Omega$ are supposed to be spatially sectionwise constant, $\chi(\lambda, z) = \chi_1(\lambda)$ for $z$ in section $S_1$.

The equation for $\dot{n}$ in (2.1) is a simple rate equation for the spatially averaged carrier density. It accounts for the current $I$, the spontaneous recombination $-n/\tau$, and the stimulated recombination. See Table 2 for typical ranges of the quantities.

## REFERENCES


[1] E. A. Avrutin, J. H. Marsh, and J. M. Arnold, *Modelling of semiconductor laser structures for passive harmonic mode locking at terahertz frequencies*, Int. J. Optoelectronics, 10 (1995), pp. 427–432.

[2] U. Bandelow, *Theorie longitudinaler Effekte in* 1.55 $\mu m$ *Mehrsektions DFB-Laserdioden*, Ph.D. thesis, Humboldt-Universität Berlin, Berlin, Germany, 1994.

[3] U. Bandelow, L. Recke, and B. Sandstede, *Frequency regions for forced locking of self-pulsating multi-section DFB lasers*, Opt. Comm., 147 (1998), pp. 212–218.

[4] U. Bandelow, M. Wolfrum, M. Radziunas, and J. Sieber, *Impact of gain dispersion on the spatio-temporal dynamics of multisection lasers*, IEEE J. Quantum Electronics, 37 (2001), pp. 183–189.

[5] U. Bandelow, H. J. Wünsche, B. Sartorius, and M. Mhrle, *Dispersive self Q-switching in DFB-lasers: Theory versus experiment*, IEEE J. Selected Topics in Quantum Electronics, 3 (1997), pp. 270–278.

[6] P. W. Bates, K. Lu, and C. Zeng, *Existence and persistence of invariant manifolds for semiflows in Banach space*, Mem. Amer. Math. Soc., 135 (1998).

[7] P. W. Bates, K. Lu, and C. Zeng, *Persistence of overflowing manifolds for semiflow*, Comm. Pure Appl. Math., 52 (1999), pp. 983–1046.

[8] P. W. Bates, K. Lu, and C. Zeng, *Invariant foliations near normally hyperbolic invariant manifolds for semiflows*, Trans. Amer. Math. Soc., 352 (2000), pp. 4641–4676.
[9] W. Beyn, *The numerical computation of connecting orbits in dynamical systems*, IMA J. Numer. Anal., 10 (1990), pp. 379–405.
[10] K. E. Brenan, S. L. Campbell, and L. R. Petzold, *Numerical Solution of Initial-Value Problems in Differential-Algebraic Equations*, North–Holland, New York, 1989.
[11] E. J. Doedel, A. R. Champneys, T. F. Fairgrieve, Y. A. Kuznetsov, B. Sandstede, and X. Wang, AUTO97: *Continuation and Bifurcation Software for Ordinary Differential Equations*, Tech. Rep., Department of Computer Science, Concordia University, Montreal, Canada; available via anonymous ftp from http://ftp.cs.concordia.ca from the directory pub/doedel/auto, 1998.
[12] K. Engelborghs, *DDE-BIFTOOL: A Matlab Package for Bifurcation Analysis of Delay Differential Equations*, Report TW 305, Katholieke Universiteit Leuven, Leuven, The Netherlands, 2000.
[13] T. Erneux, F. Rogister, A. Gavrielides, and V. Kovanis, *Bifurcation to mixed external cavity mode solutions for semiconductor lasers subject to external feedback*, Opt. Comm., 183 (2000), pp. 467–477.
[14] W. Govaerts, Y. A. Kuznetsov, and B. Sijnave, *Numerical methods for the generalized Hopf bifurcation*, SIAM J. Numer. Anal., 38 (2000), pp. 329–346.
[15] E. M. Izhikevich, *Neural excitability, spiking and bursting*, Internat. J. Bifur. Chaos Appl. Sci. Engrg., 10 (2000), pp. 1171–1266.
[16] Y. Kuznetsov, *Elements of Applied Bifurcation Theory*, Springer-Verlag, New York, 1995.
[17] R. Lang and K. Kobayashi, *External optical feedback effects on semiconductor injection properties*, IEEE J. Quantum Electronics, 16 (1980), pp. 347–355.
[18] D. Marcenac, *Fundamentals of Laser Modelling*, Ph.D. thesis, University of Cambridge, Cambridge, UK, 1993.
[19] J. Mork, B. Tromborg, and J. Mark, *Chaos in semiconductor lasers with optical feedback: Theory and experiment*, IEEE J. Quantum Electronics, 28 (1992), pp. 93–108.
[20] C. Z. Ning, R. A. Indik, and J. V. Moloney, *Effective Bloch equations for semiconductor lasers and amplifiers*, IEEE J. Quantum Electronics, 33 (1997), pp. 1543–1550.
[21] G. L. Oppo and A. Politi, *Toda potentials in laser equations*, Z. Phys., 59 (1985), pp. 111–150.
[22] A. Pazy, *Semigroups of Linear Operators and Applications to Partial Differential Equations*, Appl. Math. Sci. 44, Springer-Verlag, New York, 1983.
[23] M. Radziunas and H.-J. Wünsche, *Dynamics of Multi-Section DFB Semiconductor Laser: Traveling Wave and Mode Approximation Models*, Preprint 713, WIAS, Berlin, Germany, 2002; submitted to SPIE.
[24] M. Radziunas, H.-J. Wünsche, B. Sartorius, O. Brox, D. Hoffmann, K. Schneider, and D. Marcenac, *Modeling self-pulsating DFB lasers with integrated phase tuning section*, IEEE J. Quantum Electronics, 36 (2000), pp. 1026–1034.
[25] J. Sieber, *Longitudinal Dynamics of Semiconductor Lasers*, Report 20, WIAS, Berlin, Germany, 2001.
[26] J. Sieber, *Longtime Behavior of the Traveling-Wave Model for Semiconductor Lasers*, Preprint 743, WIAS, Berlin, Germany, 2002; SIAM J. Appl. Dynamical Systems, submitted.
[27] J. Sieber, U. Bandelow, H. Wenzel, M. Wolfrum, and H.-J. Wünsche, *Travelling Wave Equations for Semiconductor Lasers with Gain Dispersion*, Preprint 459, WIAS, Berlin, Germany, 1998.
[28] A. A. Tager and K. Petermann, *High-frequency oscillations and self-mode locking in short external-cavity laser diodes*, IEEE J. Quantum Electronics, 30 (1994), pp. 1553–1561.
[29] B. Tromborg, H. E. Lassen, and H. Olesen, *Travelling wave analysis of semiconductor lasers*, IEEE J. Quantum Electronics, 30 (1994), pp. 939–956.
[30] B. Tromborg, J. H. Osmundsen, and H. Olesen, *Stability analysis for a semiconductor laser in an external cavity*, IEEE J. Quantum Electronics, 20 (1984), pp. 1023–1032.
[31] V. Tronciu, H.-J. Wünsche, J. Sieber, K. Schneider, and F. Henneberger, *Dynamics of single mode semiconductor lasers with passive dispersive reflectors*, Opt. Comm., 182 (2000), pp. 221–228.
[32] D. Turaev, *Fundamental obstacles to self-pulsations in low-intensity lasers*, Preprint 629, WIAS, Berlin, Germany, 2001; SIAM J. Appl. Math., submitted.
[33] A. Vanderbauwhede and G. Iooss, *Center manifold theory in infinite dimensions*, in Dynamics Reported, Vol. 1, Springer-Verlag, New York, 1992, pp. 125–163.

[34] H. Wenzel, U. Bandelow, H.-J. Wünsche, and J. Rehberg, *Mechanisms of fast self pulsations in two-section DFB lasers*, IEEE J. Quantum Electronics, 32 (1996), pp. 69–79.
[35] H. J. Wünsche, O. Brox, M. Radziunas, and F. Henneberger, *Excitability of a semiconductor laser by a two-mode homoclinic bifurcation*, Phys. Rev. Lett., 88 (2002).